



# Stöber-like method to synthesize ultradispersed Fe<sub>3</sub>O<sub>4</sub> nanoparticles on graphene with excellent Photo-Fenton reaction and high-performance lithium storage



Bocheng Qiu<sup>a</sup>, Qiaoying Li<sup>a</sup>, Bin Shen<sup>a</sup>, Mingyang Xing<sup>a,\*</sup>, Jinlong Zhang<sup>a,b,\*</sup>

<sup>a</sup> Key Lab for Advanced Materials and Institute of Fine Chemicals, East China University of Science and Technology, Shanghai 200237, PR China

<sup>b</sup> Department of Chemistry, Tsinghua University, Beijing 100084, PR China

## ARTICLE INFO

### Article history:

Received 17 April 2015

Received in revised form 9 September 2015

Accepted 29 October 2015

Available online 2 November 2015

### Keywords:

Stöber-like method

Fe<sub>3</sub>O<sub>4</sub>

Graphene

Lithium ion battery

Photo-Fenton reaction

## ABSTRACT

In this paper, we report a facile Stöber-like method to prepare the ultra-dispersed Fe<sub>3</sub>O<sub>4</sub> nanoparticles (3–8 nm) on the reduced graphene oxide (RGO) sheet by using Iron (III) acetylacetonate (Fe(acac)<sub>3</sub>) as the iron precursor. This strategy provides a facile and environmentally friendly method for the large-scale synthesis of Fe<sub>3</sub>O<sub>4</sub>/RGO without any additional reductants and organic surfactants. The prepared hybrid materials are used as the Photo-Fenton catalyst to display a high and stable performance for the recyclable degradation of methyl orange pollutant, owing to the high conversion efficiency of Fe<sup>3+</sup>/Fe<sup>2+</sup> and the magnetic property of Fe<sub>3</sub>O<sub>4</sub>. Furthermore, the hybrids also show superior lithium storage performance with large reversible capacity, excellent cyclic performance (624 mAh g<sup>-1</sup> for up to 50 charge/discharge cycles at a current density of 0.1 A g<sup>-1</sup>), and good rate capability (624 and 415 mAh g<sup>-1</sup> at 0.1 and 2.4 A g<sup>-1</sup>, respectively) as an anode material, owing to its superior electrical conductivity, high surface area, excellent electrode homogeneity and dispersity. We believe that the involved Stöber-like pre-treatment method can be further extended to prepare various metal oxides/graphene composites with promising applications across a broad range of catalysis, sensors, supercapacitors, and batteries.

© 2015 Elsevier B.V. All rights reserved.

## 1. Introduction

Graphene, a single layer of two dimensional carbon material, has been used as a highly promising and versatile building block for the design of photocatalysts [1–4], electrode materials [5–7], gas sensors [8–10], and electron devices [11–13] because of a lot of unique properties in chemistry, physics, biology and mechanics. For instance, graphene has a high surface area [14], superior mechanical properties [15], excellent mobility of charge carriers [16,17], a high thermal conductivity [18,19], and ultrathin thickness [20]. These properties make it become an ideal support to anchor the semiconductor nanoparticles, and then further improve the electrochemical performance of these semiconductors. That is because the pure metal oxides materials have poor conductivity [21], and often suffer from the volume expansion and contraction associated with Li<sup>+</sup> insertion/extraction during the charge/discharge processes

[22,23]. In addition, it is noteworthy that the ultrathin flexible graphene not only can effectively prevent the aggregation of semiconductor nanoparticles, but also can permit a higher contact area between electrolyte and electrode, thus achieving a higher lithium flux across the interface during Li<sup>+</sup> charge/discharge process [24]. In other hand, many reports demonstrated that graphene can capture the photogenerated electrons effectively, thus improving the separation efficiency between electrons and holes [3–4]. For instance, Zhang et al. reported graphene–P25 composites synthesized under hydrothermal conditions that exhibited more excellent photocatalytic activity than pure P25 for the degradation of methylene blue in aqueous solutions [2].

Recently, many graphene-based materials have been reported [25–29], and these hybrid materials have attracted much attention due to their great potential applications such as lithium ion batteries (LIBs), supercapacitors, solar cells, photocatalytic water splitting and carbon dioxide photo-reduction. Some results have shown that the size, dispersion and loading density of semiconductor nanoparticles on graphene are the key factor to improve Li<sup>+</sup> storage performance [30]. Because small particle size, good dispersion and appropriate loading content can endow the composite electrode a superior high surface area to buffer the volume change

\* Corresponding authors at: Key Laboratory for Advanced Materials and Institute of Fine Chemicals, East China University of Science and Technology, Shanghai 200237, PR China. Fax: +86 21 64252062.

E-mail addresses: [mingyangxing@ecust.edu.cn](mailto:mingyangxing@ecust.edu.cn) (M. Xing), [jlzhang@ecust.edu.cn](mailto:jlzhang@ecust.edu.cn) (J. Zhang).

of the oxides during the charge/discharge processes [31]. Besides, nanosized particles can shorten lithium path length compared with the bulk counterpart. Now, the known methods constructing the semiconductor nanoparticles in-situ grown on graphene mainly include one-pot deposition process [2] and a two-step strategy [32]. In these methods, the major problems are focused on: (1) it is difficult to control the size, the uniform dispersion, and the density of the loaded semiconductor nanoparticles [22,33,34]; (2) the introduction of organic coupling reagent and surfactant to modify the surface group of graphene oxide during the synthesis process will lead to the decrease of the conductivity of graphene and make the synthetic process become tedious, unsafe and uneconomical [35]; (3) it is also uneasy to ensure that most of the semiconductor nanoparticles are in-situ grown on the graphene sheet rather than free growth in the solution [12,36]; (4) most of the reported graphene-based materials gave an terrible aggregation of reduced graphene oxide (RGO) during the reduction process [20,37]. These potential limitations have seriously hindered the development of graphene-based materials. Hence, it is very urgent to create a method to design the nanosized and highly dispersed semiconductor particles in-situ grown on graphene.

Among the semiconductors/graphene composites,  $\text{Fe}_3\text{O}_4/\text{RGO}$  has been regarded as one of the most promising materials due to the thermal stability, magnetic property and higher theoretical  $\text{Li}^+$  storage capacities [38–43]. For instance, Qiu et al. prepared nitrogen-doped graphene/ $\text{Fe}_3\text{O}_4$  hybrids using nitrogen-rich carbon as 2D crosslinker and the catalyst showed long-life lithium storage and efficient oxygen reduction [44]. Li et al. also synthesized the three-dimensional (3D) Hierarchical  $\text{Fe}_3\text{O}_4/\text{graphene}$  composites using a simple in situ hydrothermal method as catalyst for the application of the lithium ion batteries and drug delivery and supplied higher specific capacities and the excellent loading of rhodamine B (RhB) [39]. Herein, we design a facile Stöber-like method to prepare the highly dispersed  $\text{Fe}_3\text{O}_4$  nanoparticles (3–8 nm) in situ growth on graphene sheet by using iron (III) acetylacetonate ( $\text{Fe}(\text{acac})_3$ ) as the iron precursor. The prepared  $\text{Fe}_3\text{O}_4/\text{RGO}$  composites not only possess highly dispersed  $\text{Fe}_3\text{O}_4$  nanoparticles (3–8 nm), ultrathin graphene ( $\leq 4$  layers) and a high surface area of  $\sim 199.8 \text{ m}^2 \text{ g}^{-1}$ , but also exhibit superior and stable Photo-Fenton activity, and very excellent reversible lithium storage capacity.

## 2. Experimental

### 2.1. Materials

All chemicals, including  $\text{NaNO}_3$  (AR),  $\text{H}_2\text{SO}_4$  (AR),  $\text{KMnO}_4$  (AR),  $\text{H}_2\text{O}_2$  (AR), HCl (AR), concentrated ammonia solution ( $\sim 28 \text{ wt}\%$ ), iron (III) acetylacetonate  $\text{Fe}(\text{acac})_3$ , acetonitrile (AR), ethanol (AR) and  $\text{Fe}_3\text{O}_4$  powders (AR) were used as received without any further purification. Graphite powders ( $74 \mu\text{m}$ ) were purchased from Qingdao Jinrilai Graphite Co., Ltd., and ultrapure water was used for all experiments.

### 2.2. Synthesis of graphene oxide (GO)

Graphene oxide (GO) was synthesized from natural graphite powder using a modified Hummers methods [45]. Typically, 1 g graphite powders and 0.5 g  $\text{NaNO}_3$  were mixed with 25 mL concentrated  $\text{H}_2\text{SO}_4$  in an ice bath under vigorous stirring for 2 h. 3 g  $\text{KMnO}_4$  was added slowly into the mixture while the temperature was kept from exceeding  $5^\circ\text{C}$ , then the temperature of the system was heated to  $35^\circ\text{C}$  and maintained for 2 h. Afterwards, 40 mL of water was slowly added and then the mixture was heated at  $98^\circ\text{C}$  for 1 h. 140 mL of water and 40 mL of 30%  $\text{H}_2\text{O}_2$  were added to the solution at the end of reaction. The suspension was then repeat-

edly centrifuged and washed with 5% HCl solution to remove the residual salts. The wet graphene oxide was freeze-dried at  $60^\circ\text{C}$  for 24 h.

### 2.3. Synthesis of the $\text{Fe}_3\text{O}_4/\text{RGO}$ composites

By using the Stöber method, it is possible to achieve excellent control of the particle size, narrow size distribution, smooth spherical morphology of the resulting silica or other particles [46,47]. Thereby, we developed a modified Stöber-like method to achieve the highly-dispersed  $\text{Fe}_3\text{O}_4$  nanoparticles in situ growth on the graphene. Acetonitrile was used as the co-solvent to improve the solubility of  $\text{Fe}(\text{acac})_3$  in the mixed solvent [48]. The brief steps are as follows: 15 mg GO powders were dispersed in a mixed solvent containing 75 mL ethanol and 25 mL acetonitrile in an ultrasound bath for 90 min, and then 0.1 mL of  $\text{NH}_3\cdot\text{H}_2\text{O}$  was added into the suspension at room temperature. After stirring for 30 min, 10 mL  $\text{Fe}(\text{acac})_3/\text{ethanol}$  ( $0.1 \text{ mol L}^{-1}$ ) was added slowly into the above solution and then continue stirring for another 30 min. The suspension was maintained at  $60^\circ\text{C}$  for 36 h to form the amorphous  $\text{Fe}_3\text{O}_4$  nanoparticle pre-growth on the GO sheets. Subsequently, the resulting products were collected by centrifugation, washed with ethanol, and dried at  $40^\circ\text{C}$  in a vacuum oven. The as-prepared products were characterized to be the amorphous  $\text{Fe}_3\text{O}_4/\text{GO}$  composites. Finally, the crystalline  $\text{Fe}_3\text{O}_4/\text{RGO}$  composites were obtained by treating the  $\text{Fe}_3\text{O}_4/\text{GO}$  at  $500^\circ\text{C}$  for 2 h under a flow of  $\text{N}_2$ , and the heating rate is a rate of  $1.5^\circ\text{C min}^{-1}$ . For comparison, commercial  $\text{Fe}_3\text{O}_4$  powders and RGO were mixed by a physically mixing method, which was denoted as the “M- $\text{Fe}_3\text{O}_4/\text{RGO}$ ”.

### 2.4. Characterization

X-ray diffraction (XRD) patterns of all samples were collected in the range  $5\text{--}80^\circ$  ( $2\theta$ ) using a RigakuD/MAX 2550 diffract meter (Cu K radiation,  $\lambda = 1.5406 \text{ \AA}$ ), operated at 40 kV and 100 mA. The morphologies were characterized by transmission electron microscopy (TEM, JEM2000EX). The surface morphologies were observed by field emission scanning electron microscopy (FESEM, NOVA NanoSEM450). The particle size distribution curve was derived from 100 of  $\text{Fe}_3\text{O}_4$  nanoparticles. Raman measurements were performed at room temperature using Raman microscopes (Renishaw, UK) under the excitation wavelength of 532 nm. BET surface area measurements were carried out by  $\text{N}_2$  adsorption at 77 K using an ASAP2020 instrument. Thermogravimetric and differential thermal analyses were conducted on a Pyris Diamond TG/DTA (PerkinElmer) apparatus at a heating rate of  $20^\circ\text{C min}^{-1}$  from 40 to  $800^\circ\text{C}$  in air flow.

### 2.5. Photo-Fenton reaction

The photocatalytic activity of each catalyst was evaluated by in terms of the degradation of methyl-orange (MO, 10 mg/L), methylene blue (MB, 10 mg/L) and Rhodamine B (RhB, 10 mg/L). The  $\text{Fe}_3\text{O}_4/\text{RGO}$  composites powder or commercial  $\text{Fe}_3\text{O}_4$  powder was added into a 50 mL quartz reactor containing 50 mL MO solution. Prior to reaction, the initial pH value of the MO solution was adjusted to 3.5, with 0.1 M HCl, respectively. Fenton reaction was initiated by adding a known concentration of  $\text{H}_2\text{O}_2$  (1.2 mL, 30 wt%) to the solution. A 300 W Xe lamp (with AM 1.5 air mass filter) was used as a simulated solar light source. At the given time intervals, the analytical samples were taken from the mixture and immediately centrifuged before filtration through a  $0.22 \mu\text{m}$  millipore filter to remove the photocatalyst. The filtrates were analyzed by recording variations in the absorption in UV–vis spectra of MO using a Cary 100 ultraviolet visible spectrometer. For the cycle experi-

ment, after the first reaction, samples were centrifuged, repeatedly washed with water, dried at 40 °C under vacuum for 12 h, and then continued the next photocatalytic reaction.

### 2.6. Electrochemical measurements

The electrochemical experiments were carried out in coin-type cells. All the electrodes were prepared by mixing the hybrids, carbon black (Super-P), and poly-(vinyl difluoride) (PVDF) at a weight ratio of 80:10:10 to form a slurry in *N*-methyl-2-pyrrolidinone (NMP), which was coated onto a copper foil (99.6%). Pure lithium foils were used as counter and reference electrodes. The electrolyte was consisted of a solution of LiPF<sub>6</sub> (1 M) in ethylene carbonate (EC)/dimethyl carbonate (DMC) (1:1, in weight percent). The cells were assembled in an Ar-filled glove box with the concentrations of moisture and oxygen below 1 ppm. The electrochemical performance was tested on a LAND CT2001A battery test system in the voltage range of 0.01–3.00 V versus Li<sup>+</sup>/Li at room temperature Experimental Details.

## 3. Results and discussion

Nanosized and highly dispersed Fe<sub>3</sub>O<sub>4</sub> particles in situ grown on graphene were prepared by a Stöber-like method. The overall synthesis mechanism includes a two-steps reaction process (Scheme 1). Firstly, Fe(acac)<sub>3</sub> slowly hydrolyzed into Fe<sub>3</sub>O<sub>4</sub> crystal seeds, then Fe<sub>3</sub>O<sub>4</sub> seeds nucleated, grew on the surface of graphene oxide (GO) through a Stöber-like process. The next thermal treatment in N<sub>2</sub> atmosphere induced the crystallization of amorphous Fe<sub>3</sub>O<sub>4</sub> nanoparticles and the reduction of GO.

The high-resolution transmission electron microscope (HRTEM) images of the amorphous Fe<sub>3</sub>O<sub>4</sub>/GO composites exhibit the highly dispersed Fe<sub>3</sub>O<sub>4</sub> nanoparticles with a size of 3–4 nm on the surface of GO sheets ( $\leq 2$  layers) (Fig. 1a,b). There is no naked GO sheet or free Fe<sub>3</sub>O<sub>4</sub> nanoparticles appearing in the TEM images of Fe<sub>3</sub>O<sub>4</sub>/GO. Furthermore, the HRTEM image shows the absence of crystal lattices of Fe<sub>3</sub>O<sub>4</sub> (Fig. 1b), which discloses that these Fe<sub>3</sub>O<sub>4</sub> nanoparticles are in situ pre-growth on the surface of GO sheets and have not been well crystallized during the Stöber-like pre-treatment. The X-ray diffraction (XRD) patterns and the Raman spectra all further reveal the amorphous nature of Fe<sub>3</sub>O<sub>4</sub> nanoparticles (Fig. 2a,b), owing to the absence of characteristic peaks of crystallized Fe<sub>3</sub>O<sub>4</sub>. The high and sharp diffraction peak detected at  $2\theta$  between 9° and 11° in Fig. 2a is indexed to (001) of GO sheets (Fig. 2a), indicating the Stöber-like pre-treatment cannot change the morphologies and characteristics of the GO. Moreover, the Raman spectra further confirm the GO sheet during the Stöber-like process has not been reduced (Fig. S1), because the intensity ratio of D/G bands in the Raman spectra between GO and amorphous Fe<sub>3</sub>O<sub>4</sub>/GO composites is almost unchanged (0.94 vs 0.95). These results suggest that these amorphous Fe<sub>3</sub>O<sub>4</sub> nanoparticles are selectively pre-growth on the surface of GO sheets rather than free growth in the solution during the Stöber-like process, which is very important to ultimately achieve the in situ growth of Fe<sub>3</sub>O<sub>4</sub> nanocrystals on the surface of RGO sheets.

After the thermal treatment of amorphous Fe<sub>3</sub>O<sub>4</sub>/GO composites under N<sub>2</sub> atmosphere at 500 °C, the crystalline Fe<sub>3</sub>O<sub>4</sub>/RGO composites are obtained. The strong XRD diffraction peaks of Fe<sub>3</sub>O<sub>4</sub>/RGO composites are completely consistent with the peaks of commercial Fe<sub>3</sub>O<sub>4</sub> nanoparticles (Fig. 2a), indicating that the Fe<sub>3</sub>O<sub>4</sub> nanocrystals are well crystallized through the thermal treatment. The average crystal size of the Fe<sub>3</sub>O<sub>4</sub> nanoparticles is estimated around 8 nm by using Scherrer's formula. The presence of characteristic peaks in Raman spectra also confirms the generation of highly crystallized Fe<sub>3</sub>O<sub>4</sub> on the graphene (Fig. 2b). In addition, the

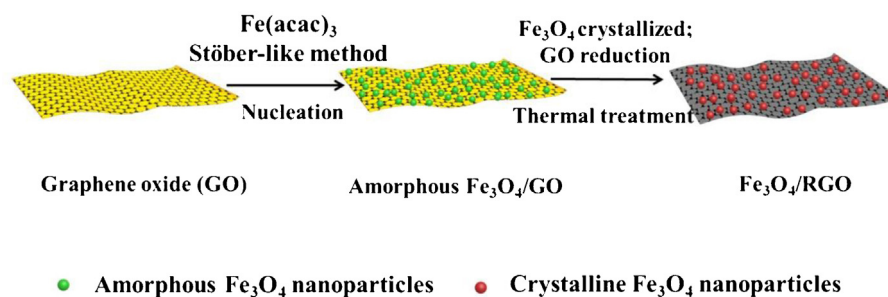
typical (001) reflection at  $2\theta = 11.3^\circ$  of the Fe<sub>3</sub>O<sub>4</sub>/RGO composites disappears, indicating the successful reduction of GO under the thermal treatment (Fig. 2a). After the thermal treatment, the obvious increasement of the intensity ratio of D/G bands in the Raman spectra further confirms the reduction of GO (Fig. S1) [49]. These results suggest the reduction of GO sheet and the crystallization of Fe<sub>3</sub>O<sub>4</sub> nanoparticles are proceed simultaneously during the high temperature thermal treatment. Moreover, the 2D band of Fe<sub>3</sub>O<sub>4</sub>/RGO composites at 2640 cm<sup>-1</sup> implies that RGO exists as a single layer in the hybrid [50]. The field emission scanning electron microscopy (FESEM) images of Fe<sub>3</sub>O<sub>4</sub>/RGO composites (Fig. 3a,b) show that the Fe<sub>3</sub>O<sub>4</sub> nanoparticles are uniformly distributed on the surface of graphene and give small size of less than 10 nm (3–8 nm), which is well consistent with the calculation result by using Scherrer's formula in XRD patterns.

More direct observations by TEM or HRTEM on morphology and structure of the Fe<sub>3</sub>O<sub>4</sub>/RGO composites are given in Fig. 4. The low-resolution TEM images of an individual composite exhibit a curved characteristic with a low contrast, revealing an ultrathin thickness of the RGO sheet with highly dispersed Fe<sub>3</sub>O<sub>4</sub> nanoparticles (Fig. 4a,b), which is in good agreement with the Raman results. No obvious large or aggregated Fe<sub>3</sub>O<sub>4</sub> nanoparticles are observed, indicating the Stöber-like method is very important and useful to control the Fe<sub>3</sub>O<sub>4</sub> size and achieve in situ and strong growth of Fe<sub>3</sub>O<sub>4</sub> on the graphene. A HRTEM image of Fe<sub>3</sub>O<sub>4</sub>/RGO composites (Fig. 4c) demonstrates that all the Fe<sub>3</sub>O<sub>4</sub> nanoparticles are well dispersed on the graphene and the size distribution curve of Fe<sub>3</sub>O<sub>4</sub> nanoparticles reveals an average size focused on 3–8 nm. Moreover, the edge of graphene (4 layers) can be clearly observed as indicated by the arrows in Fig. 4d. In addition, the HRTEM image of some individual Fe<sub>3</sub>O<sub>4</sub> nanoparticles displays clear crystal lattice with two kinds of spacing of 0.250 nm and 0.296 nm corresponding to the (3 1 1) and (2 2 0) plane [51–53], respectively (Fig. 4d). Elemental mapping analysis of Fe<sub>3</sub>O<sub>4</sub>/RGO composites was performed to illustrate the distribution of carbon, iron, and oxygen components in the hybrids (Fig. S2). Apparently, the carbon, iron, and oxygen components are uniformly distributed on the RGO sheet, further verifying the ultra-dispersed distribution of Fe<sub>3</sub>O<sub>4</sub> nanoparticles on the surface of RGO.

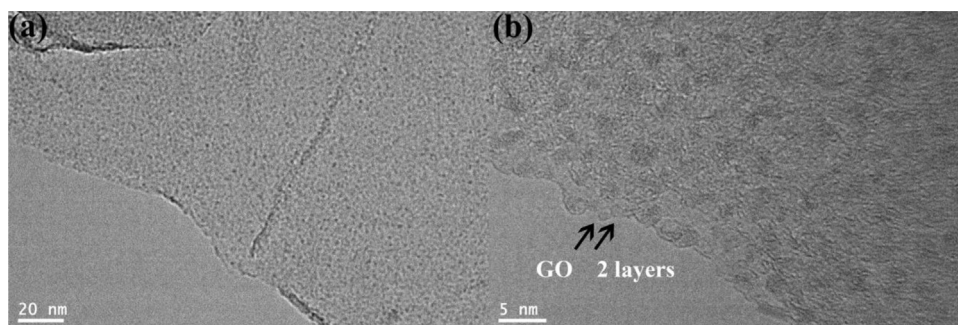
Nitrogen adsorption and desorption isotherms of Fe<sub>3</sub>O<sub>4</sub>/RGO composites show that a remarkably high specific surface area of 199.8 m<sup>2</sup> g<sup>-1</sup> together with distinct hysteresis loops close to H<sub>3</sub> type feature can be obtained in Fig. 5a. It further suggests that the Fe<sub>3</sub>O<sub>4</sub>/RGO composites have a characteristic of typical lamellar stacking [54], which is similar to the characteristic of GO (Fig. S3). In addition, such a high surface area for Fe<sub>3</sub>O<sub>4</sub>/RGO composites is vastly superior to most of Fe<sub>3</sub>O<sub>4</sub> and graphene composites reported in the past [40,55], and it also implies that the hybrid materials may have a great potential application in photocatalysis and LIBs. Thermogravimetric analysis (TGA) of Fe<sub>3</sub>O<sub>4</sub>/RGO composites was performed in air at a heating rate of 20 °C min<sup>-1</sup> to confirm the content by weight of Fe<sub>3</sub>O<sub>4</sub> in the hybrids. As shown in Fig. 5b, the TGA curve displays a big weight loss at approximately 450 °C and a constant weight above 500 °C. The major weight loss from 300 to 500 °C is about 66%, suggesting the combustion of graphene. Therefore, the content of Fe<sub>3</sub>O<sub>4</sub> in Fe<sub>3</sub>O<sub>4</sub>/RGO composites can be calculated to be approximately 34 wt%.

Photo-Fenton reaction based on ferrous ions and H<sub>2</sub>O<sub>2</sub> has been proved to be an effective technology to degrade organic pollutants by oxidation in wastewater treatment. Iron-based materials, especially Fe<sub>3</sub>O<sub>4</sub> [56], Fe<sub>2</sub>O<sub>3</sub> [57,58] and ZnFe<sub>2</sub>O<sub>4</sub> [59], are always used as the catalysts for Photo-Fenton reaction. Besides, graphene used as an electron capture agent material makes it become an ideal support to enhance the transfer and separation of photogenerated electrons and holes. The potential properties of graphene-based photocatalysts to boost the efficiency of solar energy conversion





**Scheme 1.** The overall synthetic procedure of  $\text{Fe}_3\text{O}_4/\text{RGO}$  composites.



**Fig. 1.** High-resolution TEM (HRTEM) of the amorphous  $\text{Fe}_3\text{O}_4/\text{GO}$  composites.

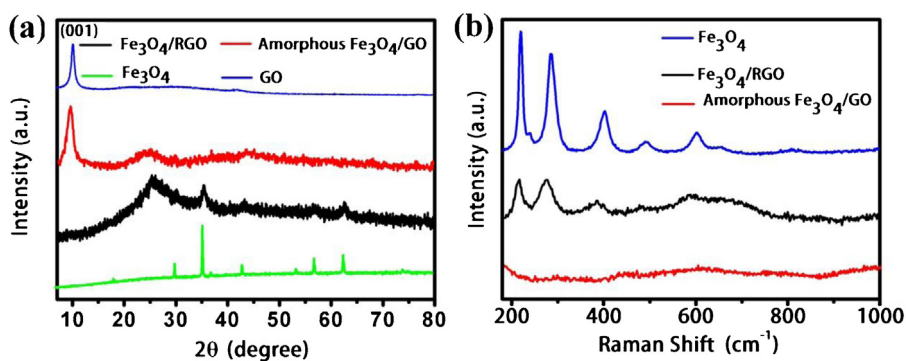


**Fig. 2.** X-ray diffraction (XRD) patterns (a) and Raman spectra (b) of the different samples.

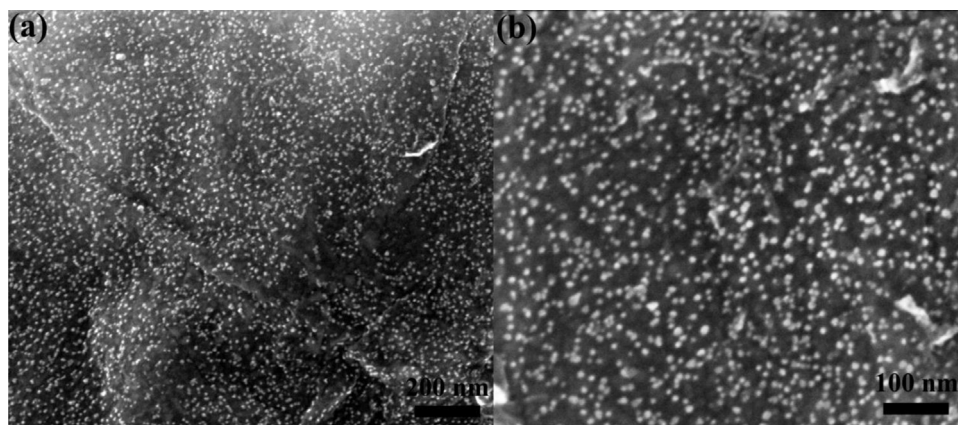


**Fig. 3.** FESEM images of  $\text{Fe}_3\text{O}_4/\text{RGO}$  composites (a, b).

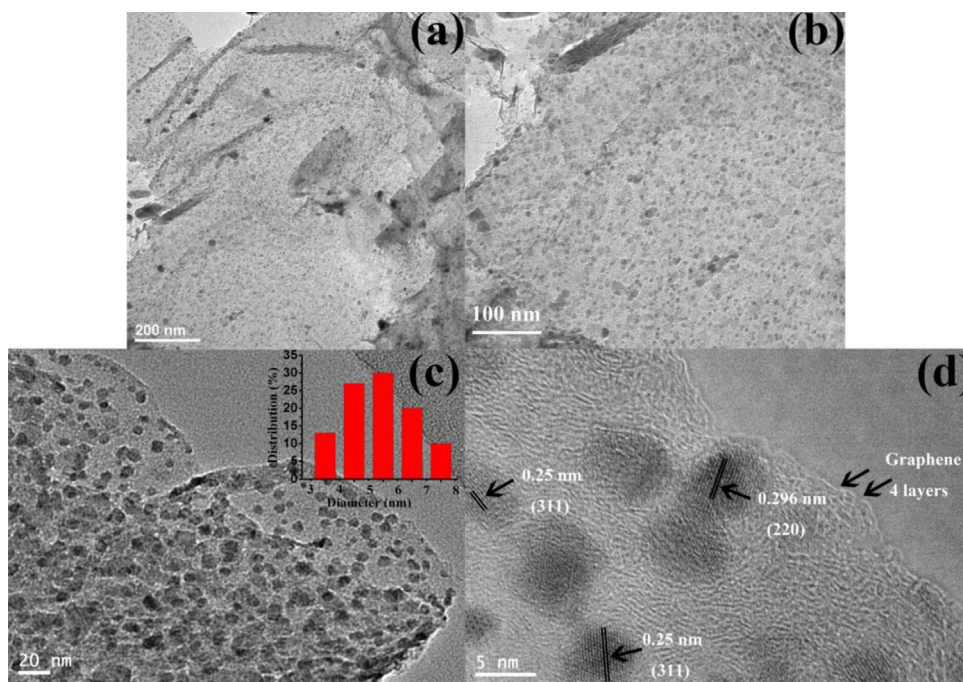


**Fig. 4.** TEM images (a, b) and HRTEM images (c, d) of Fe<sub>3</sub>O<sub>4</sub>/RGO composites. Inset of (c) is the corresponding particle size distribution of the loaded Fe<sub>3</sub>O<sub>4</sub> nanoparticles derived from 100 of Fe<sub>3</sub>O<sub>4</sub> nanoparticles in (c).

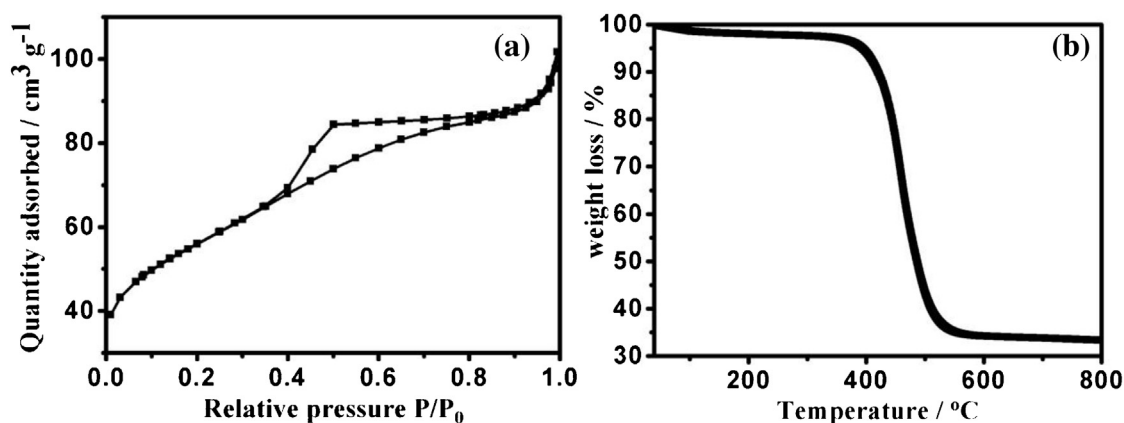


**Fig. 5.** Nitrogen adsorption and desorption isotherms of Fe<sub>3</sub>O<sub>4</sub>/RGO composites (a). Thermogravimetric analysis (TGA) curves of Fe<sub>3</sub>O<sub>4</sub>/RGO composites in air from 40 to 800 °C with a heating rate of 20 °C min<sup>-1</sup> (b).

have been explored. In this paper, the solar-driven Fenton reaction of the Fe<sub>3</sub>O<sub>4</sub>/RGO composites was conducted in the presence of H<sub>2</sub>O<sub>2</sub>, by monitoring the change in optical absorption of a methyl-orange solution (MO, 10 mg/L, Fig. 6a). In the first cycle reaction, the Fe<sub>3</sub>O<sub>4</sub>/RGO catalyst shows super-high Photo-Fenton activity and 98% of the MO molecules are degraded in 30 min. After 4 cycles, the catalyst still maintains the high Photo-Fenton activity (90%). In order to eliminate the effect of the adsorption of catalyst, the adsorption capacity of MO in the dark for Fe<sub>3</sub>O<sub>4</sub>/RGO composites has been investigated (Fig. 6a, iii<sub>1</sub> curve). It can be found that Fe<sub>3</sub>O<sub>4</sub>/RGO composites exhibit a relatively common adsorption capacity of MO (55%) in the dark for 30 min owing to the high surface area of catalyst. In addition, the photocatalytic reaction in the absence of catalyst has been investigated (Fig. S4). It can be seen that the effect of the dye self-sensitization is very weak. Therefore, it can be deduced that the high Photo-Fenton activity is caused by the Photo-Fenton reaction rather than the adsorption. In a control experiment, the commercial Fe<sub>3</sub>O<sub>4</sub> powders were used as the

Photo-Fenton reagent to test its activity and cycle performance. As shown in Fig. 6a, the commercial Fe<sub>3</sub>O<sub>4</sub> powders have a quickly diminishing Photo-Fenton activity and demonstrate a very low Photo-Fenton activity (20%) after 4 cycles. Because it is very easy for the pure Fe<sub>3</sub>O<sub>4</sub> powders to generate the iron cement (Fe(OH)<sub>3</sub>), which leads to the catalyst deactivation and low conversion efficiency of Fe<sup>3+</sup>/Fe<sup>2+</sup> [60]. On the contrary, the cycle conversion process of Fe<sup>3+</sup>/Fe<sup>2+</sup> for Fe<sub>3</sub>O<sub>4</sub>/RGO is persistent and stable. Because under the solar light irradiation, the photo-generated electrons from the dye and Fe<sub>3</sub>O<sub>4</sub> can transfer to the graphene and the Fe<sup>3+</sup> can easily capture the electrons to form Fe<sup>2+</sup>, then the Fe<sup>2+</sup> can continue react with H<sub>2</sub>O<sub>2</sub> to form the Fe<sup>3+</sup> and OH<sup>•</sup> on the surface of graphene to degrade the dye molecules (Fig. 6b). The generated Fe<sup>3+</sup> can be reduced to Fe<sup>2+</sup> again by the electron concentrated on the surface of graphene to keep the cycle of Fe<sup>3+</sup>/Fe<sup>2+</sup>. Moreover, the Fe<sub>3</sub>O<sub>4</sub>/RGO composites also show the excellent Photo-Fenton activity of degrading other dyes such as MB and RhB (Fig. 6c). Such high Photo-Fenton activity for Fe<sub>3</sub>O<sub>4</sub>/RGO composites is ascribed to the

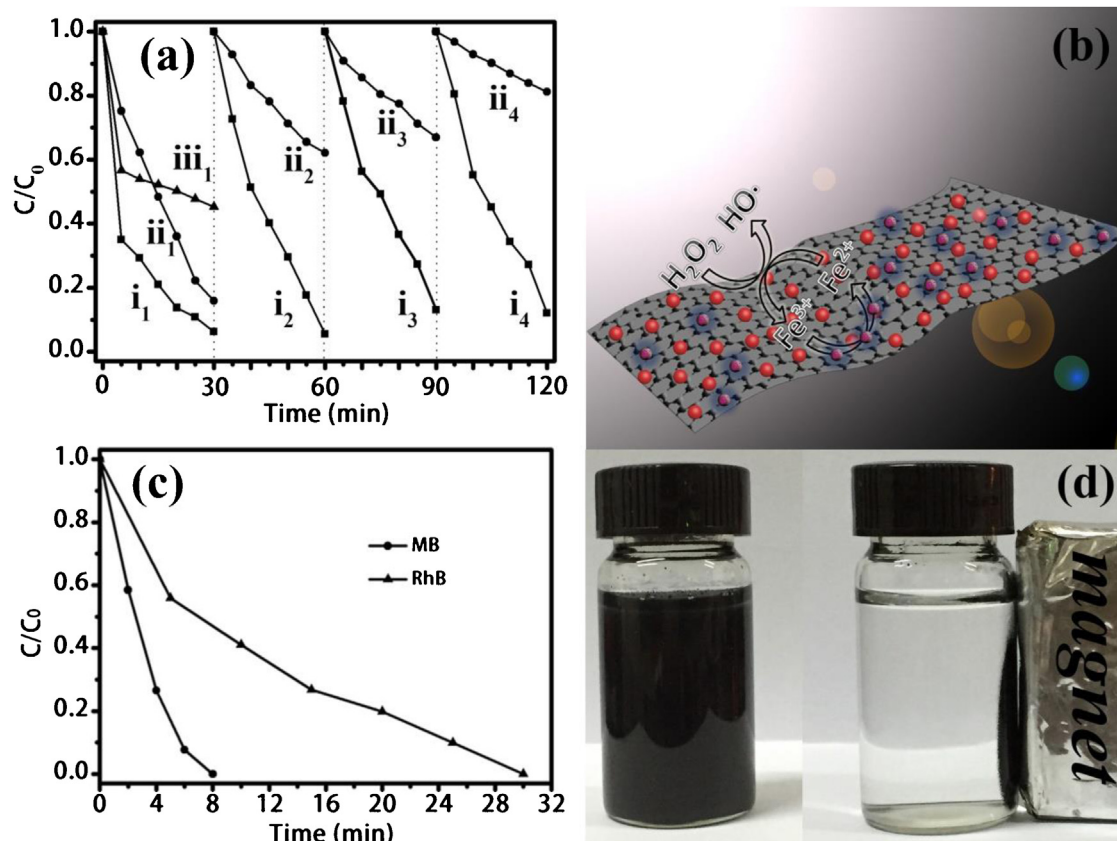


**Fig. 6.** Cycle test (i<sub>1</sub>–i<sub>4</sub>:  $\text{Fe}_3\text{O}_4/\text{RGO}$ ; ii<sub>1</sub>–ii<sub>4</sub>: commercial  $\text{Fe}_3\text{O}_4$  powders; iii<sub>1</sub>:  $\text{Fe}_3\text{O}_4/\text{RGO}$  in the dark) for the solar-driven degradation of methyl-orange (50 mL MO, 10 mg/L) under simulated solar light irradiation (with an AM 1.5 air mass filter, 1.2 mL 30 wt%  $\text{H}_2\text{O}_2$ , the initial pH was 3.5) (a). Photo-Fenton reaction mechanism of  $\text{Fe}_3\text{O}_4/\text{RGO}$  (b). Photo-Fenton degradation of (50 mL methylene blue (MB, 10 mg/L), 50 mL Rhodamine B (RhB, 10 mg/L)) (c). The magnetic separation property of  $\text{Fe}_3\text{O}_4/\text{RGO}$  photocatalyst (d).

high conversion efficiency of  $\text{Fe}^{3+}/\text{Fe}^{2+}$  and the good conductivity of RGO. In addition to the high Photo-Fenton activity, the magnetic property of  $\text{Fe}_3\text{O}_4$  gives this composites good performance in magnetic separation for the Photo-Fenton reaction. We investigated the magnetic separation properties of the  $\text{Fe}_3\text{O}_4/\text{RGO}$  photocatalyst, as shown in Fig. 6d. The catalyst can be easily and rapidly separated from the reaction solutions, which indicates its convenience for the recycle. In addition, we have used the UV–vis absorption spectroscopy to investigate the degree of mineralization. The complete mineralization is very difficult to achieve in the rapid degradation of dyes. As shown in Fig. S5, part of the MO solution has been mineralized and most of the MO solution has been decolorized. However, the degree of mineralization can be improved through the extension of reaction time.

To further verify the stability of the  $\text{Fe}_3\text{O}_4/\text{RGO}$  photocatalyst in the cycle experiment of Photo-Fenton reaction, the TEM and FESEM analyses of  $\text{Fe}_3\text{O}_4/\text{RGO}$  composites after 4 cycles were conducted, as shown in Fig. 7a,b. The TEM image shows that all the  $\text{Fe}_3\text{O}_4$  nanoparticles still ultradispersed on the graphene after 4 times cycles (Fig. 7a). Importantly, the size of  $\text{Fe}_3\text{O}_4$  nanoparticles still keeps the initial size and the RGO presents the ultrathin sheet structure. Furthermore, we also obtained the similar result of highly dispersed  $\text{Fe}_3\text{O}_4$  nanoparticles on the RGO surface in the FESEM image of Fig. 7b and the unchanged crystal structure of  $\text{Fe}_3\text{O}_4/\text{RGO}$  in Fig. S6. The above results further confirm the excellent stability of  $\text{Fe}_3\text{O}_4/\text{RGO}$  composites in structural, optical, electronic and chemical properties even after 4 cycles Photo-Fenton reaction.

In addition to the high Photo-Fenton activity, the  $\text{Fe}_3\text{O}_4/\text{RGO}$  composites also show high performance in lithium storage due to the strong coupling effects between  $\text{Fe}_3\text{O}_4$  nanoparticles and

graphene. To demonstrate the effectiveness of the unique structure of  $\text{Fe}_3\text{O}_4/\text{RGO}$  composites in improving electrochemical performance, the hybrid materials were used as an anode material to be investigated by the galvanostatic charge-discharge measurement. The charge-discharge voltage profiles from the first to fiftieth cycles at a current density of  $0.1 \text{ A g}^{-1}$  were shown in Fig. 8a. In the first discharge step,  $\text{Fe}_3\text{O}_4/\text{RGO}$  composites present an extended/long voltage plateau at about 0.8 V, followed by a sloping curve down to the cut off voltage of 0.01 V, which is a typical characteristic of voltage trend for the  $\text{Fe}_3\text{O}_4$  electrode [38]. The first charge/discharge step delivers a special discharge capacity of  $1452 \text{ mAh g}^{-1}$  and a charge capacity of  $878.9 \text{ mAh g}^{-1}$  with the initial coulombic efficiency of 60%. This initial capacity loss could potentially be ascribed to the formation of a solid electrolyte interphase (SEI) layer on the electrode surface during the first discharge step. After 50 charge/discharge cycles, the  $\text{Fe}_3\text{O}_4/\text{RGO}$  composites still demonstrate a reversible capacity as high as  $624 \text{ mAh g}^{-1}$ , which is much higher than the theoretical specific capacity of graphene ( $372 \text{ mAh g}^{-1}$ ). Moreover, it is worth stressing that the value of capacity for  $\text{Fe}_3\text{O}_4/\text{RGO}$  is based on the total mass of the  $\text{Fe}_3\text{O}_4/\text{RGO}$  and the  $\text{Fe}_3\text{O}_4$  content in  $\text{Fe}_3\text{O}_4/\text{RGO}$  only accounts for 34 wt%. However, the electrode made by the mechanically mixed composites of M- $\text{Fe}_3\text{O}_4/\text{RGO}$  only provides a reversible capacity of 1150 and  $776 \text{ mAh g}^{-1}$  at the first charge/discharge step, and the capacity quickly dropped to  $321 \text{ mAh g}^{-1}$  after 50 cycles, as shown in Fig. 8b. Fig. 8c shows the cycling performance of  $\text{Fe}_3\text{O}_4/\text{RGO}$  composites and M- $\text{Fe}_3\text{O}_4/\text{RGO}$  composites anodes at constant current densities of  $0.1 \text{ A g}^{-1}$ . Obviously, the  $\text{Fe}_3\text{O}_4/\text{RGO}$  composites electrode presents a superior and stable reversible capacity after 50 charge/discharge cycles. As a comparison, the M- $\text{Fe}_3\text{O}_4/\text{RGO}$  com-



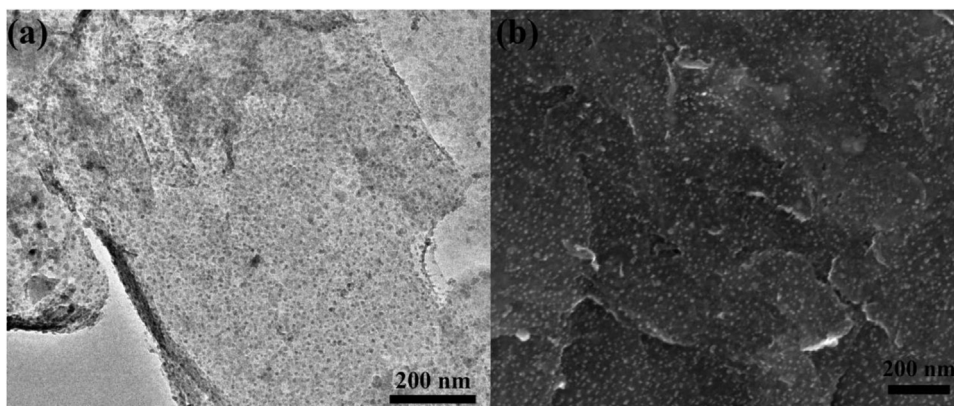


Fig. 7. TEM (a) and FESEM (b) images of  $\text{Fe}_3\text{O}_4/\text{RGO}$  after 4 cycles of Photo-Fenton reaction.

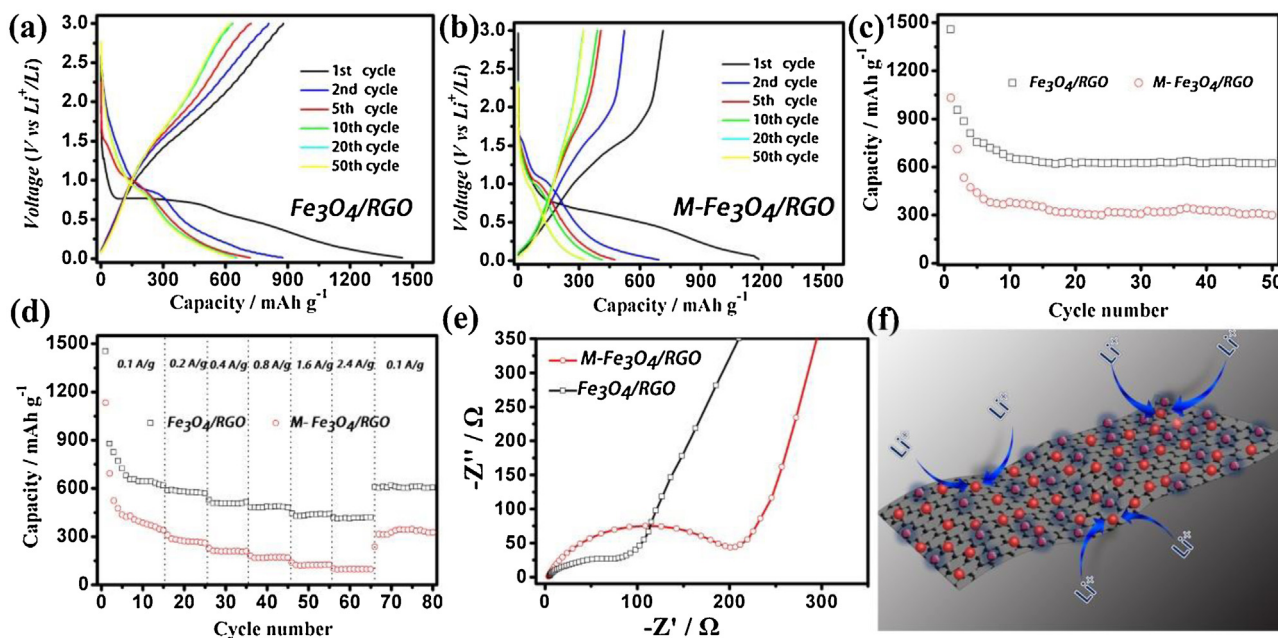


Fig. 8. The charge/discharge curve of  $\text{Fe}_3\text{O}_4/\text{RGO}$  composites (a) and mechanically mixed  $\text{Fe}_3\text{O}_4/\text{RGO}$  composites ( $\text{M-Fe}_3\text{O}_4/\text{RGO}$ ) (b) electrodes at constant current densities of  $0.1 \text{ A g}^{-1}$ . Cycling performance of  $\text{Fe}_3\text{O}_4/\text{RGO}$  composites and  $\text{M-Fe}_3\text{O}_4/\text{RGO}$  composites electrode at constant current densities of  $0.1 \text{ A g}^{-1}$  (c). Rate capability of  $\text{Fe}_3\text{O}_4/\text{RGO}$  composites and physically mixed  $\text{Fe}_3\text{O}_4/\text{RGO}$  composites at the current densities between  $0.1 \text{ A g}^{-1}$  and  $2.4 \text{ A g}^{-1}$  (d). Nyquist plots of the electrodes of  $\text{Fe}_3\text{O}_4/\text{RGO}$  sheet and mechanically mixed  $\text{Fe}_3\text{O}_4/\text{RGO}$  composites. All of the measurements were conducted using a voltage window of  $0.01\text{--}3.0 \text{ V}$  (e). Schematic representation of the electrochemical reaction path on the  $\text{Fe}_3\text{O}_4/\text{RGO}$  composites (f).

posites only keep a low discharge capacity of  $310 \text{ mAh g}^{-1}$  owing to the weak connection between  $\text{Fe}_3\text{O}_4$  nanoparticles and RGO sheets. Besides higher capacity and stable cycle capability,  $\text{Fe}_3\text{O}_4/\text{RGO}$  composites electrode also displays superior rate cycle capability. It is very clear that the  $\text{Fe}_3\text{O}_4/\text{RGO}$  composites can keep excellent cycling capability at each current density from  $0.1$  to  $2.4 \text{ A g}^{-1}$  (Fig. 8d). Remarkably, a high reversible capacity of  $415 \text{ mAh g}^{-1}$  at a high rate of  $2.4 \text{ A g}^{-1}$  for  $\text{Fe}_3\text{O}_4/\text{RGO}$  composites can be delivered. Importantly, after charge/discharge tests at the high density current, the capacity of  $\text{Fe}_3\text{O}_4/\text{RGO}$  can still return to the initial value, suggesting the high stability of  $\text{Fe}_3\text{O}_4/\text{RGO}$  composites electrode. Furthermore, the excellent cycle performance and rate capability are indicative of the ultrafast diffusion of lithium ions in the bulk of composite, due to the short diffusion path length and stability of the ultrathin RGO sheets structure. To gain further insight into the outstanding electrochemical behavior of  $\text{Fe}_3\text{O}_4/\text{RGO}$ , the alternating current (AC) impedance measurements were carried out in the Fig. 8e. Nyquist plots show that the  $\text{Fe}_3\text{O}_4/\text{RGO}$  electrode has a

much lower resistance than the  $\text{M-Fe}_3\text{O}_4/\text{RGO}$  electrode ( $84 \Omega$  vs  $200 \Omega$ ), which reveals that  $\text{Fe}_3\text{O}_4/\text{RGO}$  possesses lower contact and charge–transfer resistances.

As shown in Fig. 8f, the outstanding electrochemical performance of  $\text{Fe}_3\text{O}_4/\text{RGO}$  composites with the high capacity, stable cycling performance, and remarkable rate capacity could be ascribed to the following factors: (1) the large surface area can provide many selective pathways and enough space for the  $\text{Li}^+$  ion insertion/removal during the charging and discharging process; (2) the highly dispersed and ultra-small  $\text{Fe}_3\text{O}_4$  nanoparticles not only can drastically improve the theoretical lithium capacity for  $\text{Fe}_3\text{O}_4$ , but also can effectively reduce the diffusion length for both electrons and  $\text{Li}^+$  ions as a result of the quantum size effect; (3) the ultrathin graphene sheet can act as a good conductive substrate to improve the electron mobility and present a high degree of exposure of active sites for the lithium storage.

## 4. Conclusions

In summary, the composites of ultradispersed and nanosized  $\text{Fe}_3\text{O}_4$  particles anchored on the graphene were fabricated by a simple and interesting Stöber-like pre-treatment, which is the key technology to achieve the in situ growth of  $\text{Fe}_3\text{O}_4$  nanoparticles on the graphene in the absence of any additional reductant and organic surfactant. The obtained composites possess an ultrasmall  $\text{Fe}_3\text{O}_4$  particles size (3–8 nm), a high surface area of  $199.8 \text{ m}^2 \text{ g}^{-1}$  and ultrathin thickness ( $\leq 4$  layers). In this architecture, graphene can provide more surface-active sites and excellent routes for lithium ion storage, thereby, leading to an enhancement of the photocatalytic and electrical performance. Compared with commercial  $\text{Fe}_3\text{O}_4$  powders, the  $\text{Fe}_3\text{O}_4/\text{RGO}$  composites show the high and stable Photo-Fenton activity due to the excellent conversion efficiency of  $\text{Fe}^{3+}/\text{Fe}^{2+}$ . Besides Photo-Fenton reaction, the composites also show high reversible lithium storage capacity, excellent cycling performance, and rate capability during the discharge/charge processes in LIBs. Meanwhile, the  $\text{Fe}_3\text{O}_4/\text{RGO}$  composites are highly promising in other fields such as electrocatalysis, biological detection and gas sensor, owing to its special structure and attractive electrochemical properties. Furthermore, it is entirely possible that the employed additive-free technology of Stöber-like pre-treatment in the synthetic route can be extended as a general strategy to prepare other ultradispersed metal oxides in situ growth on the graphene.

## Acknowledgements

This work has been supported by the National Natural Science Foundation of China (21203062, 21173077, 21377038, 21237003, 21577036), the National Basic Research Program of China (973 Program, 2013CB632403), the Research Fund for the Doctoral Program of Higher Education (20120074130001), the Fundamental Research Funds for the Central Universities, and sponsored by “Chenguang Program” supported by Shanghai Education Development Foundation and Shanghai Municipal Education Commission (14CG30).

## Appendix A. Supplementary data

Supplementary data associated with this article can be found, in the online version, at <http://dx.doi.org/10.1016/j.apcatb.2015.10.053>.

## References

- [1] A. Iwase, Y.H. Ng, Y. Ishiguro, A. Kudo, R. Amal, *J. Am. Chem. Soc.* 133 (2011) 11054–11057.
- [2] H. Zhang, X. Lv, Y. Li, Y. Wang, J. Li, *ACS Nano* 4 (2009) 380–386.
- [3] M. Xing, W. Fang, X. Yang, B. Tian, J. Zhang, *Chem. Commun.* 50 (2014) 6637–6640.
- [4] Q. Xiang, J. Yu, M. Jaroniec, *Chem. Soc. Rev.* 41 (2012) 782–796.
- [5] M. Zhou, T. Cai, F. Pu, H. Chen, Z. Wang, H. Zhang, S. Guan, *ACS Appl. Mater. Interfaces* 5 (2013) 3449–3455.
- [6] M. Yan, F. Wang, C. Han, X. Ma, X. Xu, Q. An, L. Xu, C. Niu, Y. Zhao, X. Tian, *J. Am. Chem. Soc.* 135 (2013) 18176–18182.
- [7] T. Kim, G. Jung, S. Yoo, K.S. Suh, R.S. Ruoff, *ACS Nano* 7 (2013) 6899–6905.
- [8] F. Schedin, A. Geim, S. Morozov, E. Hill, P. Blake, M. Katsnelson, K. Novoselov, *Nat. Mater.* 6 (2007) 652–655.
- [9] H.Y. Jeong, D.-S. Lee, H.K. Choi, D.H. Lee, J.-E. Kim, J. Yong Lee, W.J. Lee, S.O. Kim, S.-Y. Choi, *Appl. Phys. Lett.* 96 (2010) 213103–213105.
- [10] G. Lu, L.E. Ocola, J. Chen, *Nanotechnology* 20 (2009) 445502.
- [11] K.I. Bolotin, K. Sikes, Z. Jiang, M. Klima, G. Fudenberg, J. Hone, P. Kim, H. Stormer, *Solid State Commun.* 146 (2008) 351–355.
- [12] B. Qiu, M. Xing, J. Zhang, *J. Am. Chem. Soc.* 136 (2014) 5852–5855.
- [13] A.K. Geim, K.S. Novoselov, *Nat. Mater.* 6 (2007) 183–191.
- [14] Y. Zhu, S. Murali, M.D. Stoller, K. Ganesh, W. Cai, P.J. Ferreira, A. Pirkle, R.M. Wallace, K.A. Cychosz, M. Thommes, *Science* 332 (2011) 1537–1541.
- [15] S. Bae, H. Kim, Y. Lee, X. Xu, J.-S. Park, Y. Zheng, J. Balakrishnan, T. Lei, H.R. Kim, Y.I. Song, *Nat. Nanotechnol.* 5 (2010) 574–578.
- [16] M. Xing, F. Shen, B. Qiu, J. Zhang, *Sci. Rep.* 4 (2014) 5493–5499.
- [17] B. Qiu, Y. Zhou, Y. Ma, X. Yang, W. Sheng, M. Xing, J. Zhang, *Sci. Rep.* 5 (2015) 8591–8596.
- [18] Z. Liu, Z. Li, Z. Xu, Z. Xia, X. Hu, L. Kou, L. Peng, Y. Wei, C. Gao, *Chem. Mater.* 26 (2014) 6786–6795.
- [19] Z. Xu, B. Zheng, J. Chen, C. Gao, *Chem. Mater.* 26 (2014) 6811–6818.
- [20] W. Li, F. Wang, S. Feng, J. Wang, Z. Sun, B. Li, Y. Li, J. Yang, A.A. Elzattahry, Y. Xia, *J. Am. Chem. Soc.* 135 (2013) 18300–18303.
- [21] Q. Xiang, J. Yu, J. Phy. Chem. Lett. 4 (2013) 753–759.
- [22] C. Peng, B. Chen, Y. Qin, S. Yang, C. Li, Y. Zuo, S. Liu, J. Yang, *ACS Nano* 6 (2012) 1074–1081.
- [23] Z.-S. Wu, W. Ren, L. Wen, L. Gao, J. Zhao, Z. Chen, G. Zhou, F. Li, H.-M. Cheng, *ACS Nano* 4 (2010) 3187–3194.
- [24] Z.-S. Wu, W. Ren, D.-W. Wang, F. Li, B. Liu, H.-M. Cheng, *ACS nano* 4 (2010) 5835–5842.
- [25] Z.-S. Wu, S. Yang, Y. Sun, K. Parvez, X. Feng, K. Müllen, *J. Am. Chem. Soc.* 134 (2012) 9082–9085.
- [26] L. Xiao, D. Wu, S. Han, Y. Huang, S. Li, M. He, F. Zhang, X. Feng, *ACS Appl. Mater. Interfaces* 5 (2013) 3764–3769.
- [27] G. Zhou, D.-W. Wang, L.-C. Yin, N. Li, F. Li, H.-M. Cheng, *ACS Nano* 6 (2012) 3214–3223.
- [28] X. Jiang, X. Yang, Y. Zhu, H. Jiang, Y. Yao, P. Zhao, C. Li, *J. Mater. Chem. A* 2 (2014) 11124–11133.
- [29] Y. Gu, M. Xing, J. Zhang, *Appl. Surf. Sci.* 319 (2014) 8–15.
- [30] R. Wang, C. Xu, M. Du, J. Sun, L. Gao, P. Zhang, H. Yao, C. Lin, *Small* 10 (2014) 2260–2269.
- [31] J.W. Lee, A.S. Hall, J.-D. Kim, T.E. Mallouk, *Chem. Mater.* 24 (2012) 1158–1164.
- [32] Y. Chen, B. Song, M. Li, L. Lu, J. Xue, *Adv. Funct. Mater.* 24 (2014) 319–326.
- [33] J. Zhu, D. Lei, G. Zhang, Q. Li, B. Lu, T. Wang, *Nanoscale* 5 (2013) 5499–5505.
- [34] M. Xing, J. Zhang, B. Qiu, B. Tian, M. Anpo, M. Che, *Small* 11 (2015) 1920–1929.
- [35] S. Li, D. Wu, C. Cheng, J. Wang, F. Zhang, Y. Su, X. Feng, *Angew. Chem.* 125 (2013) 12327–12331.
- [36] M. Xing, X. Li, J. Zhang, *Sci. Rep.* 4 (2014) 6341–6347.
- [37] R. Mo, Z. Lei, K. Sun, D. Rooney, *Adv. Mater.* 26 (2014) 2084–2088.
- [38] J. Su, M. Cao, L. Ren, C. Hu, *J. Phys. Chem. C* 115 (2011) 14469–14477.
- [39] X. Li, X. Huang, D. Liu, X. Wang, S. Song, L. Zhou, H. Zhang, *J. Phys. Chem. C* 115 (2011) 21567–21573.
- [40] W. Wei, S. Yang, H. Zhou, I. Lieberwirth, X. Feng, K. Müllen, *Adv. Mater.* 25 (2013) 2909–2914.
- [41] R.C. Pawar, Y. Pyo, S.H. Ahn, C.S. Lee, *Appl. Catal. B: Environ.* 176 (2015) 654–666.
- [42] R.C. Pawar, C.S. Lee, *Appl. Catal. B: Environ.* 144 (2014) 57–65.
- [43] R.C. Pawar, D.-H. Choi, C.S. Lee, *Int. J. Hydrogen Energy* 40 (2015) 767–778.
- [44] S. Liu, Y. Dong, C. Zhao, Z. Zhao, C. Yu, Z. Wang, J. Qiu, *Nano Energy* 12 (2015) 578–587.
- [45] W.S. Hummers, R.E. Offeman, *J. Am. Chem. Soc.* 80 (1958) 1339.
- [46] K. Esumi, T. Hosoya, A. Suzuki, K. Torigoe, *J. Colloid Interf. Sci.* 226 (2000) 346–352.
- [47] R. Vacassy, R.J. Flatt, H. Hofmann, K.S. Choi, R.K. Singh, *J. Colloid Interf. Sci.* 227 (2000) 302–315.
- [48] W.-F. Ma, Y. Zhang, L.-L. Li, L.-J. You, P. Zhang, Y.-T. Zhang, J.-M. Li, M. Yu, J. Guo, H.-J. Lu, C.-C. Wang, *ACS Nano* 6 (2012) 3179–3188.
- [49] Y. Huang, D. Wu, S. Han, S. Li, L. Xiao, F. Zhang, X. Feng, *ChemSusChem* 6 (2013) 1510–1515.
- [50] V. Etacheri, J.E. Yourey, B.M. Bartlett, *ACS Nano* 8 (2014) 1491–1499.
- [51] A.Y. Lin, J.K. Young, A.V. Nixon, R.A. Drezek, *Small* 10 (2014) 3246–3251.
- [52] C.-H. Ho, C.-P. Tsai, C.-C. Chung, C.-Y. Tsai, F.-R. Chen, H.-J. Lin, C.-H. Lai, *Chem. Mater.* 23 (2011) 1753–1760.
- [53] N. Fontañón-Troita, B. Rivas-Murias, B. Rodríguez-González, V. Salgueiriño, *Chem. Mater.* 26 (2014) 5566–5575.
- [54] F. Dong, Z. Wang, Y. Li, W.-K. Ho, S.C. Lee, *Environ. Sci. Technol.* 48 (2014) 10345–10353.
- [55] Q. An, F. Lv, Q. Liu, C. Han, K. Zhao, J. Sheng, Q. Wei, M. Yan, L. Mai, *Nano Lett.* 14 (2014) 6250–6256.
- [56] L. Xu, J. Wang, *Environ. Sci. Technol.* 46 (2012) 10145–10153.
- [57] Z.-M. Cui, Z. Chen, C.-Y. Cao, L. Jiang, W.-G. Song, *Chem. Commun.* 49 (2013) 2332–2334.
- [58] B. Qiu, M. Xing, J. Zhang, *J. Mater. Chem. A* 3 (2015) 12820–12827.
- [59] Y. Fu, X. Wang, *Ind. Eng. Chem. Res.* 50 (2011) 7210–7218.
- [60] J.I. Nieto-Juarez, T. Kohn, *Photochem. Photobiol. Sci.* 12 (2013) 1596–1605.